Journal of
Synchrotron Radiation

ISSN 0909-0495

Received 13 November 2008
Accepted 11 June 2009

Focusing, collimation and flux throughput at the IMCA-CAT bending-magnet beamline at the Advanced Photon Source

Irina Koshelev,[a]*‡ Rong Huang,[a] Timothy Graber,[b] Mati Meron,[b] J. Lewis Muir,[a] William Lavender,[c] Kevin Battaile,[a] Anne M. Mulichak[a] and Lisa J. Keefe[a]

[a]IMCA-CAT, The Center for Advanced Radiation Sources, University of Chicago, IL 60637, USA, [b]ChemMatCARS, The Center for Advanced Radiation Sources, University of Chicago, IL 60637, USA, and [c]Biological, Chemical, and Physical Sciences Department, Illinois Institute of Technology, Chicago, IL 60616, USA. E-mail: ikoshelev@anl.gov

The IMCA-CAT bending-magnet beamline was upgraded with a collimating mirror in order to achieve the energy resolution required to conduct high-quality multi- and single-wavelength anomalous diffraction (MAD/SAD) experiments without sacrificing beamline flux throughput. Following the upgrade, the bending-magnet beamline achieves a flux of 8×10^{11} photons s^{-1} at 1 Å wavelength, at a beamline aperture of 1.5 mrad (horizontal) × 86 µrad (vertical), with energy resolution (limited mostly by the intrinsic resolution of the monochromator optics) $\delta E/E = 1.5 \times 10^{-4}$ (at 10 kV). The beamline operates in a dynamic range of 7.5–17.5 keV and delivers to the sample focused beam of size (FWHM) 240 µm (horizontally) × 160 µm (vertically). The performance of the 17-BM beamline optics and its deviation from ideally shaped optics is evaluated in the context of the requirements imposed by the needs of protein crystallography experiments. An assessment of flux losses is given in relation to the (geometric) properties of major beamline components.

Keywords: X-rays; bending magnet; sagittal focusing; collimation; flux throughput; macromolecular crystallography.

1. Introduction

The Industrial Macromolecular Crystallography Association Collaboration Access Team (IMCA-CAT) was created to satisfy the pharmaceutical industry's need for a synchrotron-based macromolecular crystallography tool and to facilitate research in drug design and development. To solve the *de novo* three-dimensional atomic structure of a protein, phase information for the X-rays scattered by a protein crystal is essential. This information can be obtained from multiwavelength anomalous dispersion (MAD) measurements, provided that an X-ray beam of sufficient intensity (requiring a synchrotron source) and high monochromaticity is available. The IMCA-CAT bending-magnet beamline was upgraded to achieve the energy resolution required to conduct high-quality multi- and single-wavelength anomalous diffraction (MAD/SAD) experiments, without sacrificing beamline flux throughput. The upgrade made possible MAD phasing protein crystallography measurements for elements with electron binding energies within the energy range 7.5–17.5 keV (for example, platinum, gold or mercury) with the majority of experiments utilizing selenomethionine (*K*-edge of Se) or bromine (*K*-edge of Br). The requirements of macromolecular crystallography for beam monochromaticity, small beam size (dictated by the typical size of a protein crystal) and high flux density, combined with the properties of the X-ray source presented by the Advanced Photon Source (APS), provided the main constraints and considerations in the choice of optical components and their configuration for the 17-BM bending-magnet upgrade.

The Advanced Photon Source is a third-generation synchrotron facility with high-brilliance insertion devices, capable of delivering a highly collimated beam of up to 5×10^{13} photons s^{-1} $(100\ mA)^{-1}$ at 10 keV, using a Si (111) monochromator. The flux delivered by a bending-magnet source is lower than that delivered by an undulator device; however, a bending-magnet source on a low-emittance third-generation storage ring may deliver a beam of a flux density and an energy resolution comparable with an unfocused undulator beamline, if the bending-magnet beamline optics are designed to achieve appropriate focusing. Moreover, a bending-magnet beamline can be operated over a wide range of X-ray energies while keeping the thermal loads on beamline components virtually constant, thus reducing the deterioration

‡ Present address: The Center for Advanced Radiation Sources, University of Chicago, IL 60637, USA.

of the optical components' performance and minimizing thermal stabilization times. Therefore, for applications where the highest achievable flux density is not mandatory and where high stability and the ability to rapidly scan over a broad energy range are important, a bending-magnet source at a third-generation synchrotron is very attractive.

The APS bending-magnet source has a critical energy of $\sim$19.5 keV, and an r.m.s. source size of $\sigma_x \simeq 91$ µm horizontally and $\sigma_y \simeq 25$ µm vertically (APS, 2009). The horizontal angular width of the white-beam radiation fan is 6 mrad, of which 2 mrad is accepted by 17-BM beamline apertures. The vertical angular profile for the bending-magnet source is closely approximated by a Gaussian distribution with an r.m.s. divergence of σ_y (mrad) = $(565/\gamma)(E_c/E)^{-0.425}$ (Margaritondo, 1988), where E is the photon energy, E_c is the critical energy of the bending magnet, and γ is the relativistic gamma-factor of the ring. For the APS, $\gamma \simeq 13700$; thus, given a 17-BM bending-magnet beamline chromatic range of 7.5–17.5 keV, this vertical divergence (r.m.s.) varies from 62 µrad to 43 µrad, while the Darwin width of the Si (111) reflection changes from 35.3 µrad to 14.7 µrad, respectively. Thus, in order to achieve an energy resolution limited only by the monochromator's Si (111) crystal optics while accepting most of the flux delivered by the source in the vertical direction, vertical collimation of the beam upstream of the monochromator is required. Furthermore, in order to achieve maximum flux on the sample, and match the FWHM beam size to the average crystal dimensions of 50–250 µm for a typical 17-BM protein crystallography project, vertical and horizontal focusing of the beam is absolutely necessary. A disadvantage of the aggressive focusing (primarily in the horizontal direction) which is required to deliver maximum flux onto the focal spot is that it may limit macromolecular protein crystals which can be used to collect high-quality data sets, owing to (potential) overlap of closely spaced diffraction spots for crystals with a long unit cell, for highly divergent beams.

The design of the 17-BM beamline follows a proven scheme successfully working at other beamlines conducting materials and life sciences research (Lang *et al.*, 1999; Bilsborrow *et al.*, 2006; Cianci *et al.*, 2005; Pohl *et al.*, 2001; Wang *et al.*, 2008; Roth *et al.*, 2002; Borsboom *et al.*, 1998; Ferrer *et al.*, 1998). The optics scheme chosen for the 17-BM beamline includes a vertically collimating mirror (bent flat) upstream of the monochromator, and a vertically focusing mirror (also bent flat) following the monochromator. Horizontal focusing is achieved by sagittal bending of the second crystal of the monochromator. This provides superb focusing at the price, however, of flux losses at higher energies. The assessment of flux losses owing to bending properties of the beamline optics is a significant factor in consideration of the operating energy range for the 17-BM beamline. Following the upgrade, the theoretical operation envelope for IMCA's bending-magnet beamline specifies delivery of a monochromatic beam in the energy range 7–17.5 keV, with a flux of $\sim 10^{12}$ photons s^{-1} (12 keV) and $\delta E/E \simeq 1.3 \times 10^{-4}$, to a focal spot of (FWHM) 60 µm (V) × 200 µm (H) at the sample location, 54 m from the source. Important beamline parameters like angular beam profile, energy resolution and flux throughput will be discussed in relation to the bending properties of the collimating mirror and the sagittally focusing monochromator. The performance of the 17-BM beamline optics and its deviations from ideally shaped optics will be evaluated in the context of requirements imposed by the needs of protein crystallography experiments.

2. Optical layout

The main optical components of the 17-BM beamline are two cylindrically bent flat mirrors which provide collimation and vertical focusing, and a Si (111) sagittally focusing monochromator. A schematic layout of the beamline is shown in Fig. 1. The beamline includes two enclosures, the optics station and the experiment endstation. All focusing components are located in the optics station, providing a $\sim$(1:1) demagnification ratio. As a result of the large distances from the source to the optical components, and from the optical components to the sample, combined with the small r.m.s. size of the X-ray source, a focused beam size (especially in the vertical direction) depends mainly on the quality of the optical components, thus putting strict constraints on the optical surface finish and mirror benders' designs.

The first optical component on the beamline is the collimating mirror. To collimate the incoming radiation, the mirror is cylindrically bent to focus the beam at infinite distance (*i.e.* its focal length equals the source–mirror distance). The collimating mirror accepts a large portion of the vertical beam size without compromising energy resolution because the beam divergence, following the mirror, is significantly smaller than the Darwin width of the monochromator crystal, for the energy range of interest. Although highly collimated, the X-ray beam after the collimating mirror is a polychromatic beam and cannot be used directly for macromolecular crystallography experiments, since the bandwidth of the bending-magnet radiation (Schwinger, 1949) is much larger then the $\sim 10^{-4}$ bandwidth required by a MAD protein crystallographic data collection experiment.

The reduction of the bandwidth of the X-ray beam to that required by protein crystallography experiments and the selection of desired X-ray beam energy is performed by the

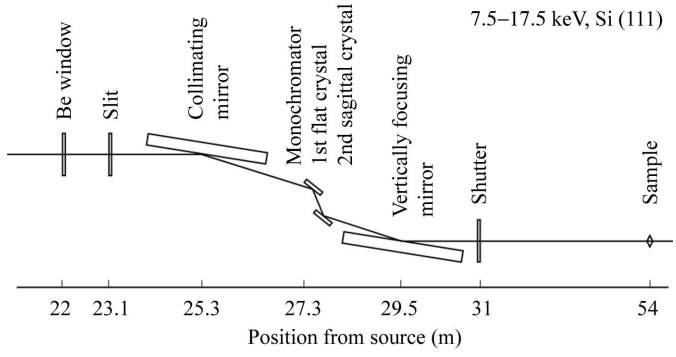

Figure 1
Schematic of the 17-BM optical layout.

Table 1
Optical parameters for the 17-BM mirrors.

The mirrors were characterized at the X-ray Optics Metrology Laboratory at the APS using a long trace profilometer and a figure interferometer. Meridional slope errors are given for a mirror mounted in the bender with enabled gravitational compensators. Measurements are performed on 90% of the mirror length extension.

Component	Substrate	Coating (Å)	Roughness (Å)	Slope errors (μrad)	Size (L × W × T) (mm)	Radius of curvature (m)
Collimating mirror	Si	500 (Pd), 100 (Cr)	2.62 ± 0.35	3.1	1040 × 90 × 45	16866
Vertically focusing mirror	ULE	1000 (Pd), 100 (Cr)	2.32 ± 0.3	1.4	1000 × 80 × 50	16333

second optical component at the beamline, a double-crystal sagittally focusing monochromator (DCM). For the highly collimated beam delivered by the first mirror, the first crystal of the DCM provides energy resolution limited only by the crystal's inherent Darwin width. The second crystal returns the beam to a horizontal trajectory and, serving as a Bragg reflector (Howell & Hastings, 1983), is sagittally bent to provide horizontal focusing of the wide bending-magnet radiation fan on the sample. Since the focal length is defined by both the bending radius and the angle of incidence to the surface (which varies with energy), the ability to dynamically adjust the bending radius of the sagittal crystal over a broad range is necessary.

The third optical component is another cylindrically bent flat mirror, which performs a dual function. Its primary role is to vertically focus the beam onto the sample. This is necessary since the vertical size of the beam following the collimating mirror is of the order of a few millimeters. Thus, vertical focusing is necessary in order to match the vertical beam size to a typical sample size. Almost as important is high harmonic rejection. A double-crystal monochromator passes not only an X-ray beam of selected fundamental energy E_0 but also those harmonics which are permitted by selection rules for Si (111), at energies of $3E_0$, $4E_0$ *etc.* (see *International Tables for Crystallography*, 2002). In order to eliminate this unwanted radiation, a low-pass filter component such as an X-ray mirror is used. The first mirror provides some harmonic rejection, while the second greatly improves on it.

The combination of independent vertical and horizontal focusing components on the beamline provides the flexibility to focus the beam at the desired location and to tailor the vertical and horizontal beam size to the experimental requirements.

3. Optical components

3.1. Collimating mirror

The first optical component of the 17-BM beamline is a water-cooled collimating mirror (Rosenbaum-Rock bender design, LR Design, Scottsdale, AZ, USA). The collimating mirror was fabricated by InSync (Albuquerque, NM, USA) from silicon and coated with palladium. The mirror is located 25.3 m from the X-ray source and positioned so that the X-rays impinge on the mirror at a grazing angle of 3 mrad, which defines the critical energy for the mirror at 21.5 keV. The mirror subtends ∼118 μrad of the vertical beam, thus accepting ∼2/3 of the total beam at 1 Å wavelength.

The collimating mirror's geometrical, physical and optical parameters are shown in Table 1. The mirror has height, angle and bend adjustments; details of a similar mirror's bender design (without side cooling system) are given elsewhere (Rosenbaum *et al.*, 2006). The mirror was glued with EPO-TEK 301-2 to plates, which are connected to the bender mechanism, capable of providing continuous adjustment of bending moments so the mirror can be changed from flat to convex or concave, up to a bending radius of curvature of 2 km. The mirror has an indirect side water cooling system consisting of directly cooled copper blocks, clamped to the side surfaces of the mirror. Indium foil of thickness 0.01″ is placed between the mirror's side surface and the copper blocks for improved heat transport properties. The mirror bender is provided with a spring-type gravitational compensation mechanism. It has seven pairs of springs, which are mounted with one side to centers of copper cooling blocks and with the other side attached to the mirror cage.

A perfectly shaped collimating mirror will reduce the divergence of the beam to a value determined solely by the transverse extent of the source and the distance of the collimating optics from the source. In the case of the 17-BM beamline, this minimal divergence is ∼2 μrad (FWHM). Random slope errors of contemporary mirrors are of comparable size and the resulting divergence is considerably smaller than the angular acceptance of the monochromator's crystals. What are (potentially) of greater concern are non-random mirror deformations, such as those owing to sagging under the force of gravity. This will be discussed at length in §4.1 and in Appendix *A*.

3.2. Double-crystal monochromator

The second optical component at the 17-BM beamline is a 35 mm fixed beam offset double-crystal monochromator (DCM), which was designed by Daresbury Laboratory and manufactured by Vacuum Generators (UK).

The vertical position of the first monochromator crystal is fixed, thus allowing the beamline to operate only at a single fixed angle of the collimating mirror. The monochromator employs two silicon crystals in a (111) orientation. The first crystal of the DCM is a flat Si (111) crystal with indirect cooling, the second crystal is a sagittally bent Si (111) mounted in a bender of Rosenbaum-Rock design (LR Design, Scottsdale, AZ, USA). Both Si (111) crystals are mounted on a

Table 2
Optical parameters for the 17-BM crystals.

The crystals were characterized at the X-ray Optics Metrology Laboratory at the APS using a topography test unit diffractometer (TTUD). The rocking curve width at FWHM is given for a crystal mounted in the TTUD with minimal mounting stress. A Si (333) reflection at 8 keV was used in the measurements.

Component	Substrate	Miscut (°)	Size (L × W × T) (mm)	Rocking curve width FWHM (arcsec)	Radius of curvature (m)
First crystal	Si (111)	<0.05	85 × 75 × 12	2.8	Flat
Sagittal crystal	Si (111)	<0.05	75 × 53 × 0.7 (active area)	2.7	4.3 (12398 eV), 3.1 (17500 eV)

common shaft with an angle positioning resolution of 5×10^{-5} deg (corresponding to 0.065 eV at 12.4 keV). The monochromator is adjusted for small misalignments owing to miscuts of the DCM crystals, inaccuracy of mechanical mounts and thermal expansion of the crystal mounts. The optical and geometrical parameters for the 17-BM monochromator are given in Table 2.

The first Si (111) crystal of the DCM is mounted on a copper holder plate using a Ga-In eutectic layer of approximately 10 μm thickness. The holder plate has water-cooling channels, is fabricated with high flatness and low roughness and is nickel-plated to prevent a reaction of the holder material with the Ga-In eutectic. The 12 mm-thick crystal is syton polished to a mirror finish on both the reflecting and mounting sides and is clamped to the holder using screws which allow variable torque to be applied. The torque of the screws was adjusted in the APS Topography Laboratory, using a TTUD unit (Maj *et al.*, 2006), so that mounting strains in the crystal were less than 1 arcsec over the entire crystal surface. This way of mounting provides great flexibility in minimizing the mounting strain while still providing excellent reliability in the crystal positioning. The monochromator, with the crystal mounted on the holder as described above, is capable of delivering energy reproducibility better then 0.2 eV.

In addition to attaining an accurate and stable setting of the Bragg angle for the first crystal, this way of crystal mounting and cooling minimizes the distortion of the crystal's rocking curve under the thermal load. Indeed, the collimating mirror in this beamline set-up serves not only for collimation and energy filtering but also as a power filter. At the design 3 mrad operating angle, the Pd-coated Si mirror absorbs more than 50% of the total power load, delivering onto the crystal ∼40 W, at a beamline aperture of 100 μrad (V) × 1.5 mrad (H) and APS ring current of 100 mA. This power is transferred efficiently to the crystal's holder, and the residual thermal broadening of the crystal's rocking curve under this power load is less than 2.5 μrad.

The second crystal of the DCM is a sagittally bent Si (111). The bender is mounted on a double stage with the capability to move vertically and laterally along the beam in order to preserve a fixed exit beam when the energy of the monochromator is changed. The design principles of a sagittal bender with a four-point loading geometry are described in detail by Howell & Hastings (1983), Rosenbaum *et al.* (1992) and Ice & Sparks (1994). The sagittal (horizontal) focusing is essential for a bending-magnet beamline to collect a significant portion of the horizontal beam. However, it may cause loss of flux owing to deviation of the sagittally bent crystal planes from the Bragg condition. This will be discussed at length in §4.2.

3.3. Vertically focusing mirror

Unlike the collimating mirror, the vertical focusing mirror is only exposed to a monochromatic beam (with negligible power loading) and it is used on the beamline to focus the beam vertically, and as an additional low-bandpass filter. The mirror bender was designed and manufactured by Oxford Danfysik (UK), while the mirror was fabricated by InSync. The mirror's geometrical, physical and optical parameters are given in Table 1. The mirror bender applies equal bending moments to the ends of the mirror *via* stainless steel weak link plates. The mirror's bend radius can be changed dynamically from concave to convex and the mirror's height and angle of incidence can be adjusted. For routine operation the mirror angle is set to 3 mrad. Due to the endstation configuration, the angle of incidence for both mirrors cannot be modified during operations. As a result, the cut-off energy for both mirrors is 21.5 keV, which limits the beamline's low-energy operating limit to about 7.5 keV, with a harmonic contamination of ∼0.7%.

The vertically focusing mirror is equipped with spring-loaded gravitational compensators which minimize the effects of the mirror's gravitational sagging, thus decreasing non-random slope errors delivered by the mirror. The FWHM of the vertical beam profile, which was obtained with the monochromator utilizing flat crystal optics at the beamline's full aperture of 86 μrad (V) × 1.5 mrad (H) and was focused vertically at the sample location, is 120 μm, compared with the FWHM of 60 μm calculated for the beam profile delivered by ideal optics. This allows one to conclude that the total broadening owing to surface figure errors and slope errors for both collimating mirrors is 105 μm (FWHM), translating to an r.m.s. slope error for both mirrors of ∼2 μrad, indicating a high quality of surface finish and exceptional mechanical performance of the grazing-incidence vertically focusing X-ray components.

4. Focusing and related beamline throughput issues

The beamline throughput is defined as the fraction of radiation within the specified energy bandwidth present in the original bending-magnet source beam that is delivered into

the focal spot at the sample location. The initial flux, for the purpose of the theoretical evaluation, is the flux of radiation, within the theoretical energy bandwidth, that is passing through IMCA's standard beamline aperture of 0.086 mrad (V) × 1.5 (H) mrad. The beamline throughput at the IMCA bending-magnet beamline is primarily determined by two of the optical components, namely the collimating mirror and the sagittally focusing crystal of the DCM.

4.1. Collimating mirror

IMCA's collimating mirror is bent by applying constant and equal bending moments to the clamped ends of the flat rectangular mirror of constant thickness. In this bending configuration the mirror is bent into a cylindrical shape. As is well known, the shape required for perfect collimation is parabolic. However, for practical radii of curvature ($\sim 10^4$ m) and mirror lengths ($\sim$1 m) the difference between a cylindrical and parabolic profile is negligible, resulting in slope errors in the sub-picoradian range. Other factors may cause larger deviations, resulting in defocus, coma, spherical aberration *etc.* (Ehrenberg, 1949; Padmore *et al.*, 1996; Underwood, 1977; Howells *et al.*, 2000). The third-order aberration owing to gravitational sagging of the mirror can be larger than others, amounting to slope errors of tens of microradians. The gravitational sagging of a mirror can be mitigated by increasing the thickness of the mirror, fabricating mirrors with non-uniform thickness, or using strategically placed springs gravitational compensators (Ice, 1996; Howells *et al.*, 2000). The IMCA collimating mirror springs gravitational compensation system was adjusted at the APS X-ray Optics Metrology Laboratory using the long trace profilometer (LTP) unit. Final r.m.s. slope errors over the central 90% of the mirror extension are given in Table 1.

The collimating mirror slope profile was tested *in situ* at the beamline by moving slits of size 300 µm (V) × 500 µm (H) in front of the mirror and by measuring the position of the beam reflected by the collimating mirror, after the DCM with flat optics. The deflection of the beam is proportional to the local slope error of the mirror, averaged over the footprint of the beam (which sets a high limit on the spatial frequencies which can be detected). For the *in situ* measurements the collimating mirror was used with installed and enabled gravitational compensation and water-cooling system. The beam aperture has been chosen small enough to ensure that the errors owing to beam divergence are negligible, the beam footprint is small compared with the length of the mirror, and that the thermal loads on the collimating mirror (0.18 W) and the first Si (111) crystal of the DCM (0.07 W) are small enough to cause no observable distortion of these optical components.

The measured position of the beam reflected by the collimating mirror as a function of the scanning slit position is shown in Fig. 2. The abscissa on the top of the graph represents distance, where the beam impinges the mirror's surface, from the center of the mirror. The abscissa on the bottom of the graph represents the angle position of the beam aperture (as seen from the source), corresponding to the above-indicated beam position on the mirror's surface. The calculated beam position reflected by an ideal parabolically bent mirror is a linear function. The deviation of the beam position after being reflected by the (IMCA) collimating mirror from the calculated beam position for the ideal parabolically bent mirror is a cubic function of the beam position at the mirror surface, which is consistent with aberrations caused by gravitational sagging of the collimating mirror.

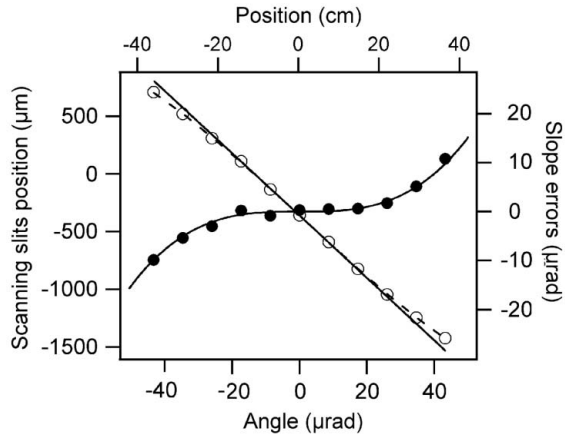

Figure 2
The displacement of the beam reflected by the collimating mirror as a function of the beam position on the mirror, top axis (or corresponding beam angular position, bottom axis), is shown in open circles. The solid line shows a linear fit to the experimental data and represents the beam position, reflected by the ideal mirror. The deviation of the measured mirror slope errors from a parabolic (ideal) mirror is shown in closed circles. A fit to this data by a model of an ideally smooth mirror with gravitational sag is given by the solid line.

Calculations of the aberrations owing to gravitational sag of the mirror (also found elsewhere: Howells *et al.*, 2000; Ice, 1996; Padmore *et al.*, 1996) and the calculations of the angular profile of a beam reflected from a mirror distorted by gravitational sagging are described in detail in Appendix *A*. For the actual mirror configuration the solution of the Euler–Bernoulli beam equation has to account for the point loads of cooling blocks and gravitational compensators of the collimating mirror. The solution of this problem is outside the scope of this paper; however, the simple model (presented in Appendix *A*) describes well the experimental data. As shown by Howells *et al.* (2000), by Ice (1996) or by Padmore *et al.* (1996) and emphasized in Appendix *A*, for a mirror in the shape of a rectangular beam the gravitational sag can be characterized by a single physical parameter which depends only on the dimensions and the material properties of the mirror. This parameter has dimensions of length and will be referred to here as $R_{\rm GL}$ (see Appendix *A*). A least-squares fit to the experimental data shown in Fig. 2 yields $R_{\rm GL} = 18 \pm 2$ km, which is very close to the theoretical value, $R_{\rm GL} = 18.3$ km, calculated for a Si mirror of thickness 4.5 cm and length 104 cm. Therefore, it appears that gravitational compensation is not fully effective for this mirror, for reasons which are currently unclear. The data demonstrate that, for the central 35% length of the collimating mirror, slope errors (relative to an ideal cylindrically bent mirror) are less than 1 µrad, and remain less than 2 µrad if $\sim$45% of the mirror

is illuminated. However, as can be seen in Fig. 2, the non-random slope errors at the ends of the collimating mirror increase to 10 μrad, while r.m.s. slope errors measured by LTP (see Table 1) are 3.1 μrad with actual slope errors, measured at the ends of the scanned (by LTP) collimating mirror surface, being 5–8 μrad. This difference may be attributable to the changes in the gravitational compensation system during transportation and installation (mounting) of the collimating mirror as well as to additional weight of the cooling system of the collimating mirror owing to water circulating in the cooling channels.

The angular profiles of the X-ray beam reflected by the 4.5 cm-thick collimating mirror (IMCA's) and by an ideal mirror, calculated (as described in the Appendix *A*) for the APS bending-magnet source parameters (APS, 2009) at 1 Å wavelength, are shown in Fig. 3. The throughput of the collimating mirror was calculated using a vertical aperture of 86 μrad (a typical value for the IMCA beamline operating conditions). For comparison, angular profiles of the X-ray beam reflected by a 10 cm-thick (minute deviations from ideal parabolic surface of the mirror) and 2 cm-thick (strong deviation from the ideal mirror) collimating mirror, calculated under the same conditions, are also shown in Fig. 3. In addition, Fig. 3 displays the FWHM of the diffraction curve for Si (111) at 1 Å, calculated in the dynamical approximation. The theoretical angular beam profiles, given in Fig. 3, are convoluted with the angular size of the source. The divergence of a beam reflected by an ideal mirror is determined by this size alone. As can be seen, decreasing the mirror thickness does not increase the width of the central part of the beam profile, but rather contributes to long extending tails. Since these can be removed afterwards using slits (aperture), the mirror focusing ability, as measured by the FWHM of the reflected beam, does not suffer.

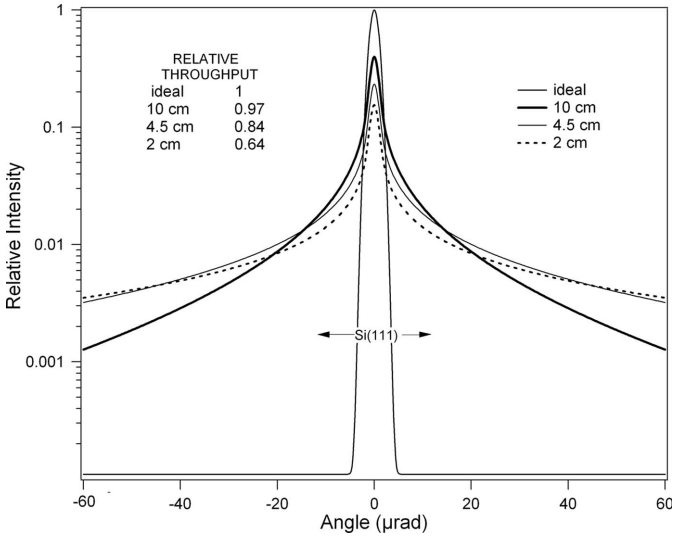

Figure 3
The angular beam profile reflected by a collimating mirror is calculated for a mirror length of 104 cm and mirror thicknesses of 10 cm, 4.5 cm, 2 cm, and an ideal mirror at 1 Å and the APS bending-magnet X-ray source parameters. For comparison, the FWHM of a Si (111) Darwin curve at 1 Å is shown by the arrows. The insert on the graph shows the relative flux throughput after the collimating mirror of length 104 cm and of given thickness to the ideal mirror for a beamline vertical acceptance angle of 86 μrad.

In the case of ideal beamline optics, with unlimited transverse extent, the slope errors of the collimating mirror do increase the bandpass of the X-ray beam thus decreasing the peak flux, but do not influence the total flux. However, since real optics has limited transverse extent and includes finite-size apertures, slope errors may result in flux losses.

The energy and spatial distributions of the delivered beam are correlated, with the beam fractions which are reflected at different angles (relative to beam center) and transmitted through the DCM (owing to different energies) lying away from the beam center along the beam trajectory. For sufficiently large angles these beam fractions may be cut by apertures, with a resultant flux loss. For a beam at 1 Å wavelength and beamline vertical aperture of 86 μrad, the flux throughput loss, in our case, owing to the gravitational sag of the Si collimating mirror (4.5 cm-thick, 104 cm in length) is ∼15% (compared with practically no losses for a 10 cm-thick collimating mirror or 35% for a mirror thickness of 2 cm).

4.2. Sagittal crystal

For sagittal focusing, when the source and the focal spot are located at distances of F_1 and F_2 from the sagittal optics, respectively, the radius of curvature R of the optical component is defined by

$$\frac{1}{F_1}+\frac{1}{F_2}=2\frac{\sin\theta}{R}, \qquad (1)$$

where θ is the incidence angle of the X-rays impinging on the sagittal optical component. For crystal optics this is the Bragg angle (Sparks *et al.*, 1981; Ice & Sparks, 1984). To satisfy Bragg conditions, the angle of incidence for the sagitally focusing crystal has to change with energy. Consequently, the radius of curvature of the crystal changes dynamically as a function of energy.

When a thin elastic plane is bent to a sagittal radius of curvature $R_{\rm sag}$, bending strains will occur not only along the principal (sagittal) bending direction but also (owing to Poisson coupling) in the transverse direction (Timoshenko & Woinowsky-Krieger, 1959; Sparks *et al.*, 1981). This transverse strain will cause the crystal to bend into a saddle shape in the longitudinal direction to an anticlastic radius of curvature $R_{\rm ant}$, such that for an unconstrained crystal $R_{\rm sag}/R_{\rm ant}=-\nu$, where ν is the Poisson ratio. The effect of anticlastic bending cannot be eliminated, but it can be minimized by choosing a crystal of appropriate design (Sparks *et al.*, 1981; Kushnir *et al.*, 1993). The design of the 17-BM sagittal crystal is based on the numerical calculations and the experimental data presented by Kushnir *et al.* (1993): a geometrical ratio of the length to the width for the thin web (thin portion) of the sagittal crystal was set to the 'golden ratio' of 1.42.

Being bent, the crystal planes deviate from the Bragg condition at locations away from the crystal's center. The transverse deviation, which is caused directly by the sagittal

bending, is proportional to the horizontal beam divergence and depends on the sagittal optics demagnification ratio (Sparks *et al.*, 1980). For the 17-BM horizontal aperture of 1.5 mrad, focal length of ∼27 m and sagittal optics demagnification ratio of 1:1, this effect is negligible. In addition, the longitudinal deviation caused by the anticlastic effect is non-negligible and it does (especially at higher energies) limit the monochromator's flux throughput. The anticlastic curvature of the bent crystal can be measured by translating it through a beam of small divergence and measuring the position of the rocking curve satisfying the Bragg condition for the second crystal. The position of the rocking curve as a function of the second crystal's displacement from the center is shown in Fig. 4(*a*). The measurements were performed at a wavelength of 1 Å with the beam focused horizontally at the sample location. The beam aperture was located upstream of the monochromator, ∼23 m from the source, and had a size of 300 µm (V) and 500 µm (H). From the experimental data, presented in Fig. 4(*a*), it can be concluded that at 1 Å the effective sagittal crystal size, at which deviation of the rocking curve from the position of the rocking curve in the center of the crystal is less than half of the Darwin width, is ∼12 mm.

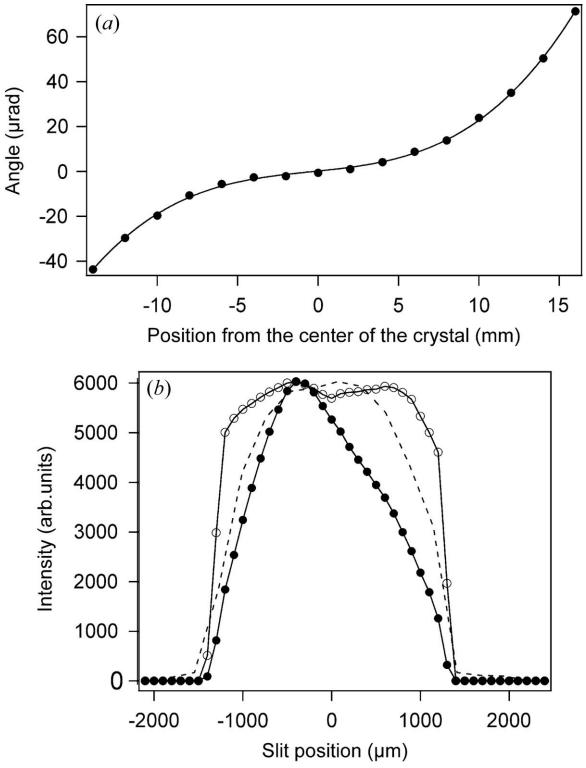

Figure 4
(*a*) Position of the rocking curve of the sagittally bent Si (111) crystal as a function of the distance from the center of the sagittal crystal. Measurements are performed at 1 Å in the sample focusing geometry. (*b*) Intensity after DCM as a function of the beam defining slit position for the Si (111) flat crystal (open circles), and the sagittally bent Si (111) crystal (closed circles). The dashed curve represents calculated DCM flux throughput for the sagittal focusing with anticlastic curvature as measured experimentally and is shown in (*a*). Measurements and calculations were performed at 1 Å and in the sample focusing geometry (when applicable).

Table 3
The manifestation of the anticlastic effect for 17-BM sagittal crystal optics at a beamline acceptance of 86 µrad (V) × 1.5 mrad (H).

The anticlastic profile of the Si (111) sagittal crystal was measured as a function of sagittal crystal bending radius, which is required for the X-ray beam of different energy to be focused at the sample.

Energy (eV)	Beam footprint (mm)	Flux throughput, calculated (%)	Darwin width (arcsec)	Sagittal radius (m)
8000	8.91	98	6.80	6.74
10000	11.13	95	5.38	5.37
12398.4	13.80	82	4.30	4.32
14000	15.59	65	3.80	3.85

Fig. 4(*b*) shows the calculated beam flux throughput after the sagitally focusing DCM with the experimentally measured anticlastic sagittal crystal shape (dashed line). This curve is compared with the experimentally measured throughput for the sagittally focusing DCM, and for a DCM with two flat crystals. A beam profile after the DCM with two flat crystals exhibits a sharp cut-off on both sides which is defined by the edges of the mirror components. The calculated curve shows flux losses owing to the sagittally bent Si (111) crystal Bragg plane deviation from the Bragg condition away from the center of said crystal. As can be seen, the expected losses of flux throughput related to the anticlastic effect of the sagittally bent crystal are smaller then those measured experimentally. The additional part of the experimentally observed losses can be attributed to a small misalignment of the sagittal crystal.

To evaluate the beamline total flux losses owing to the anticlastic effect, measurements of the anticlastic curvature for the crystal, sagitally focusing at the sample location, were performed at different energies. Calculated values of beamline throughput, based on these measurements, are given in Table 3. Here, the flux throughput represents the ratio of the calculated flux, transmitted through sagittally bent Si (111) with an experimentally measured anticlastic shape, and the theoretical flux through a pair of two ideal flat Si (111) crystals at the given energy and beamline vertical aperture of 86 µrad. In the calculations it was assumed that the anticlastic radius of curvature of the whole surface of the crystal is the same as that measured experimentally in the center of the crystal. As can be seen from Table 3, at the 17-BM beamline vertical angular acceptance of 86 µrad, anticlastic bending does not affect flux throughput at energies below 10 keV. At low energies, owing to higher Bragg angles of the crystal and the larger radius of curvatures required for the sagittal crystal to focus the beam at the sample, the length of the anticlastically bent surface of the crystal where deviation of the crystal planes are negligible from crystal planes of the ideal unbent crystal is comparable, or larger than, the beam footprint. On the contrary, for energies above 14 keV, this length is much smaller then the beam footprint; therefore, losses of the flux owing to anticlastic effects are significant. Both anticlastic bending of the sagittally focusing optics and strain induced by the sagittal bending depend on energy and are increased at higher energies. At higher energies, the crystal must be bent to a smaller radius of curvature to focus the beam sagittally, thus

increasing the curvature of the crystal in the longitudinal direction and reducing the beamline photon throughput. At the same time, owing to decreased Bragg angles at higher energies, the area of the beam footprint on the crystal increases, and the Darwin width of the crystal reflection is declining. Therefore, the fraction of the area of the crystal where the Bragg condition is being met is reduced, and this results in a reduction of the total flux.

4.3. Beamline energy resolution

The energy resolution of a beamline is determined by the resolution of the monochromator optics and by the divergence of the beam impinging on the monochromator. The energy band-pass is defined by

$$\frac{\delta E}{E} = \frac{(\delta\theta_{\rm D}^2 + \delta\theta_{\rm i}^2)^{1/2}}{\tan\theta_{\rm B}}, \qquad (2)$$

where $\delta\theta_{\rm D}$ is the Darwin width of the monochromator crystal at energy E, $\theta_{\rm B}$ is the Bragg angle at this energy, and $\delta\theta_{\rm i}$ is the FWHM beam divergence after the collimating mirror. To measure the energy resolution delivered by beamline optical components, a highly dispersive Si (555) crystal located downstream of the DCM with two flat crystals was used as an energy analyzer. The Bragg angle of the DCM crystals was changed while the intensity of the X-ray beam, diffracted by Si (555) in backscattering geometry, was measured by an ionization chamber. In this experimental geometry, Si (555) possesses a resolution of $\delta E/E = 1.9 \times 10^{-6}$, so the width of the experimentally measured band-pass curve is defined only by the Darwin width of the first Si (111) DCM crystal and by the divergence delivered by the collimating mirror. The collimating mirror was cylindrically bent until a minimal band-pass-curve width of 1.45 eV (FWHM) was achieved at 10 keV and at a beamline vertical acceptance angle of 86 µrad. The band-pass curve for this optimal mirror bend is shown in Fig. 5 [these experimental data were also presented elsewhere (Koshelev *et al.*, 2007)]; the dotted line in Fig. 5 represents the calculated band-pass curve of Si (111) after the cylindrically bent collimating mirror with calculated gravitational sag. The theoretical energy resolution was obtained by a convolution of the calculated (dynamical approximation) diffraction curve of Si (111) and the angular beam profile given by equation (10) for an ideally flat cylindrically bent collimating mirror at 10 keV. The tails of the theoretical band-pass curve are due to slope errors at the ends of the collimating mirror and can be eliminated by aperturing the beam in the vertical direction when only the central part of the mirror is illuminated. The measured energy band-pass is ∼12% larger than the theoretical value of 1.31 eV for perfect collimation which means that the beam divergence after the monochromator is increased compared with ideally shaped optics. The essential contribution to the final beam divergence can be attributed to slope errors of the collimating mirror, residual crystal mounting strains, thermal load distortion and the APS bending-magnet source size. The APS bending-magnet angular source extension of ∼2 µrad accounts for only minor residual divergence, therefore the increase of the residual beam divergence can be attributed mostly to the crystal's mounting strains and deviation of the collimating mirror shape from cylindrical owing to non-random surface figures (see Fig. 2). In the above experiment the collimating mirror can accept vertically up to 100 µrad of white beam without seriously compromising the energy resolution delivered by the beamline.

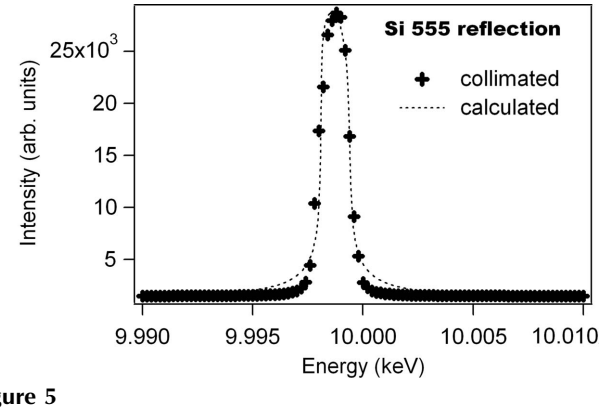

Figure 5
DCM energy scan as a function of the collimating mirror bend for the collimated (crosses) beam. The dotted line represents the calculated band-pass curve for the DCM with flat Si (111) and after cylindrically bent collimating mirror with calculated gravitational sag.

For the sagittally focusing monochromator the second crystal serves as a Bragg reflector, and the energy resolution of such a system is defined by the Darwin width of the Bragg reflection and the energy spread caused by deviation of the crystallographic planes from the Bragg condition caused by the curvature of the sagittally bent crystal (Howell & Hastings, 1983; Sparks *et al.*, 1981). In our case, the energy resolution of the sagittally focusing monochromator is not significantly different from what could be obtained using flat crystal optics.

5. Combined beamline performance

The combined beamline performance is characterized by the total flux delivered by the beamline, as well as the flux delivered into the focal spot, the design focal spot size, the beam stability *etc.* The flux delivered into the focal spot is affected by the collimating mirror, along with the sagittally focusing monochromator, while the total flux is impacted by the sagittally focusing monochromator only. Fig. 6 shows the total measured photon flux of the beam, focused vertically and horizontally at the sample, and the calculated monochromatic flux for an accepted white beam of 86 µrad (vertically) × 1.5 mrad (horizontally). The theoretical flux is calculated for ideal optical components in a paraxial approximation. The sharp cut off in the theoretical flux curve at ∼20 keV is due to the critical angle for the Pd-coated grazing-incidence vertically focusing optics. The total photon flux delivered by the beamline is lower than the calculated flux and deviates significantly from the theoretical curve at higher energies. The beamline total flux losses have contributions owing to the bending properties of the sagittally focusing optics and, to a lesser extent, strain and thermal effects in the DCM crystals.

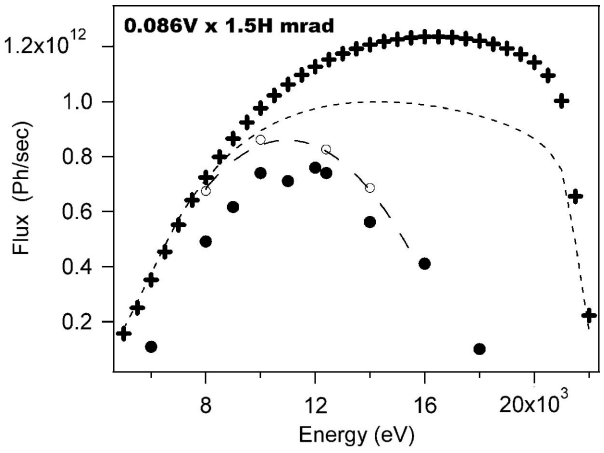

Figure 6
Total measured flux (filled circles) of the fully focused beam, theoretical flux for ideal optics (crosses) and calculated flux through the sagittally focusing DCM (open circles/dashed line) as a function of energy. Theoretical flux throughput for IMCA's collimating mirror (dotted line) with calculated gravitational sag and DCM energy bandwidth of an ideal crystal as a function of energy is also shown.

Flux losses owing to bending properties of the sagittally focusing optics are calculated using experimental data as described in §4.2. As can be seen, the dominant contribution to the beamline flux losses at higher energies can be attributed to the anticlastic effect of the sagittally bent second crystal of the DCM. The losses owing to all above-mentioned effects will become more pronounced at higher energies. The Darwin width for the crystals decreases at higher energies while the beam footprint on the monochromator crystals increases, so angular deviations, induced by mounting, bending or thermal distortion of the crystals, become more significant in comparison with the Darwin width.

For comparison, the loss of the theoretical beamline throughput at a given energy owing to gravitational sagging of the collimating mirror is also shown in Fig. 6. The throughput was calculated as in Appendix *A* for a beam of given energy and energy bandwidth, defined by the Darwin width of the crystal, for a beamline vertical aperture of 86 μrad.

The focal size of the beam is determined by the combined performance of all optical components: the sagittally bent crystal, and the collimating and vertically focusing mirrors. The beam, fully focused, has an average FWHM size of 240 μm (horizontally) × 160 μm (vertically). This is ∼15% more than the theoretical horizontal beam size of 200 μm (FWHM), and is more than double the theoretical vertical beam size of 60 μm (FWHM) calculated for ideal optics with the APS beam parameters. The difference in horizontal beam size is presumably due to a slight non-uniformity of the sagittal crystal thickness or other bending errors (like twist), while the difference in the vertical beam size is mostly due to tangential slope errors and non-random surface figure errors of the mirrors and the crystals. It was found that the contribution to the vertical beam profile broadening from the sagittal optics is comparable with the total broadening introduced by the slope errors and non-random surface figure errors of longitudinally focusing optics. This cannot be avoided. An important property of sagittally bent crystal optics is the presence of coupling between horizontal and vertical focusing (Ice & Sparks, 1984). A beam, emanating from a point source and of horizontal divergence ψ, intercepts a sagittally bent crystal at a surface with different vertical extension thus contributing to vertical beam profile broadening. On the other hand, an anticlastic effect, which is intrinsic to sagittal bending, distorts the sagittal crystal in the vertical direction and causes optical aberrations, which result in a further increase of the vertical beam size (Ice & Sparks, 1984).

One of the important characteristics of a beamline is beam stability. The spatial stability of the delivered beam is mostly determined by the mechanical stability of the optical systems and by the speed of thermal equilibration under the heat load of the X-ray source. The temperature of the collimating mirror and the monochromator's first crystal mostly stabilizes within 15–20 min from the delivery of the X-ray beam; however, it takes much longer for the monochromator's second crystal and the mounting hardware to thermally stabilize. A large fraction of the radiation incident on the monochromator first crystal is scattered. Despite substantial water-cooled shielding of the second crystal mounts, part of the radiation, scattered by the first crystal, is absorbed by crystal mounting hardware. Since the mass of this hardware is substantial, thermal equilibration times are very long. The monochromator's rocking curve position changes by ∼2 μrad over a time span of 140 h, at a fixed energy and at a constant particle beam current of 100 mA top-up mode. This introduces a long-term drift which is mitigated by the beam positioning feedback device (up to 20 μm beam position stability at the sample location).

6. Summary and conclusions

The IMCA-CAT bending-magnet beamline achieves a flux density of 4×10^{12} photons s^{-1} mm^{-2} at an energy resolution limited mostly by the intrinsic resolution of the monochromator optics. The beamline accepts a bending-magnet radiation fan of 1.5 mrad (horizontal) × 100 μrad (vertical), operating in a dynamic range of 7.5–17.5 keV, limited at the low end by the energy at which beam harmonic contamination grows beyond 0.7% and at the high end by losses of flux owing to an anticlastic effect and strains induced in the sagittally bent Si (111) crystal. Owing to the large distance between the optical components and the sample location, the size of the focused beam on the sample is determined primarily by the quality of the focusing optics and equals (FWHM) 240 μm (horizontally) × 160 μm (vertically), thus displaying outstanding performance of the optical components. The beamline delivers flux throughput with 75% efficiency at 1 Å with losses in flux mostly due to the sagittal optics anticlastic effect. Following the upgrade, the beamline performance in terms of throughput, energy resolution, focal size and stability allows successful MAD phasing of protein crystal structures and accommodates a wide variety of protein macromolecular crystallography experiments.

APPENDIX A
Angular profile of a beam reflected by gravitationally sagging mirror

When a flat rectangular mirror of a constant thickness is bent into a cylindrical shape by applying equal constant bending moments to the ends of the mirror, then, according to the theory of elasticity, the out-of plane beam y displacement is described by the Euler–Bernoulli beam equation (Timoshenko & Woinowsky-Krieger, 1959)

$$\left[EI\frac{\mathrm{d}^4y}{\mathrm{d}x^4}\right] = P, \tag{3}$$

where E is Young's modulus of the mirror, I is the area moment of inertia of the mirror's cross section and P is the distributed loading. Equation (3) is valid under the assumption that Young's modulus of the mirror and the moment of inertia of the mirror's cross section do not vary with x along the mirror length l and that y, the deflection of the mirror, is small compared with the length of the mirror. Both assumptions are well satisfied in our case. In (3) the loading of the mirror is $P = \rho gwt$, where ρ is the mirror density, g is the gravitational constant, w is the mirror width and t is the mirror height. The moment of inertia of a beam with constant cross section is given by $I = wt^3/12$ (Timoshenko & Woinowsky-Krieger, 1959). For the clamped mirror, the displacements at the two end points of the mirror equal zero, and the slopes at the mirror end points equal $l/2R$, where R is the radius of curvature provided by the two applied moments. A solution of (3), satisfying these boundary conditions, is

$$y = -\frac{1}{R_{\rm GL}}\frac{x^4}{l^2} + \left(\frac{1}{R} + \frac{1}{R_{\rm GL}}\right)\frac{x^2}{2}, \tag{4}$$

where

$$\frac{1}{R_{\rm GL}} = \frac{\rho g}{2E}\frac{l^2}{t^2}. \tag{5}$$

Here, the constant offset on the right-hand side of (4) was omitted because it does not change the subsequent analysis. Using (4), the slope errors, *i.e.* the deviation of $\mathrm{d}y/\mathrm{d}x$ of the mirror caused by gravitational sag, relative to the shape produced by an ideal parabolically bent mirror, can be calculated and compared with the actual slope errors delivered by IMCA's collimating mirror.

In the case of a collimating mirror with gravitational sagging, it is of interest to calculate how the aberration affects the angular profile of the X-ray beam, reflected by the collimating mirror. This can be calculated using geometrical ray tracing. Assume a mirror is inclined at a grazing angle θ relative to the center ray of the X-ray beam. Assume, further, a ray emanating from the source with initial location (relative to the source's center) $\Delta r_{\rm s}$ and an angular deviation (relative to the center ray) of $\Delta\theta_{\rm s}$, impinging on the surface of the mirror at a distance x from the mirror's center. The ray is reflected by the mirror described by the function $y(x)$ so that the angular displacement $\Delta\theta_{\rm i}$ after the reflection equals $\Delta\theta_{\rm i} = 2\psi - \Delta\theta_{\rm s}$, where $\psi = \mathrm{d}y(x)/\mathrm{d}x$ is the angle between the mirror's surface tangent and the x axis. When the distance d between the X-ray source and the mirror is much larger then the mirror's size l, then x can be approximated by

$$x = \frac{\Delta r_{\rm s} + \mathrm{d}\Delta\theta_{\rm s}}{\sin\theta}. \tag{6}$$

Choosing the bend radius R to eliminate any first-order dependence of $\Delta\theta_{\rm i}$ on $\Delta\theta_{\rm s}$ we find, for the case of a mirror surface described by (4),

$$\Delta\theta_{\rm i} = \frac{\Delta r_{\rm s}}{d} - \frac{1}{\left(1/R + 1/R_{\rm GL}\right)^3 R_{\rm GL} l^2}\left(\frac{\Delta r_{\rm s}}{d} + \Delta\theta_{\rm s}\right)^3, \tag{7}$$

where

$$\left(\frac{1}{R} + \frac{1}{R_{\rm GL}}\right) = \frac{\sin\theta}{2d}. \tag{8}$$

Since the contribution of the source size, $\Delta r_{\rm s}/d$, is very small in comparison with typical values of $\Delta\theta_{\rm s}$, it can be neglected to first order, leaving $\Delta\theta_{\rm i}$ as a function of $\Delta\theta_{\rm s}$ alone. The angular distribution of the bending-magnet radiation is approximated by a Gaussian (Margaritondo, 1988),

$$I(\Delta\theta_{\rm s}) = \frac{1}{(2\pi\sigma_{\rm s}^2)^{1/2}}\exp\left(-\frac{\Delta\theta_{\rm s}^2}{2\sigma_{\rm s}^2}\right), \tag{9}$$

where $\sigma_{\rm s}$ is the bending-magnet source r.m.s. divergence. Subsequently, the distribution of the reflected beam intensity as a function of $\Delta\theta_{\rm i}$ is defined by

$$I(\Delta\theta_{\rm i}) = I(\Delta\theta_{\rm s})\frac{\mathrm{d}\Delta\theta_{\rm s}}{\mathrm{d}\Delta\theta_{\rm i}}. \tag{10}$$

We would like to thank G. Rosenbaum (SER-CAT, University of Georgia) and R. Fischetti (GM/CA-CAT, ANL) for extensive and fruitful discussions on 17-BM beamline design and performance. We also would like to acknowledge the efforts of L. Assoufid, J. Qian and J. Maj (APS) on experimental support for metrology measurements performed on the 17-BM optical components. Use of the IMCA-CAT beamline 17-BM at the Advanced Photon Source was supported by the companies of the Industrial Macromolecular Crystallography Association through a contract with the Center for Advanced Radiation Sources at the University of Chicago.

References

APS (2009). *SR Source Parameters*, http://www.aps.anl.gov/Accelerator_Systems_Division/Operations_Analysis/SRSourceParameters/sourcePointResults/.

Bilsborrow, R. L., Atkinson, P. A., Bliss, N., Dent, A. J., Dobson, B. R. & Stephenson, P. C. (2006). *J. Synchrotron Rad.* **13**, 54–58.

Borsboom, M., Bras, W., Cerjak, I., Detollenaere, D., Glastra van Loon, D., Goedtkindt, P., Konijnenburg, M., Lassing, P., Levine, Y. K., Munneke, B., Oversluizen, M., van Tol, R. & Vlieg, E. (1998). *J. Synchrotron Rad.* **5**, 518–520.

Cianci, M. *et al.* (2005). *J. Synchrotron Rad.* **12**, 455–466.

Ehrenberg, W. (1949). *J. Opt. Soc. Am.* **39**, 741–746.

Ferrer, J.-L., Simon, J.-P., Bérar, J.-F., Caillot, B., Fanchon, E., Kaïkati, O., Arnaud, S., Guidotti, M., Pirocchi, M. & Roth, M. (1998). *J. Synchrotron Rad.* **5**, 1346–1356.
Howells, M. R., Cambie, D., Duarte, R. M., Irick, S., MacDowell, A. A., Padmore, H. A., Renner, T. R., Rah, S. & Sandler, R. (2000). *Opt. Eng.* **39**, 2748–2762.
Howell, M. R. & Hastings, J. B. (1983). *Nucl. Instrum. Methods Phys. Res.* **208**, 379–386.
Ice, G. (1996). *Proc. SPIE*, **2856**, 157–162.
Ice, G. E. & Sparks, C. J. (1984). *Nucl. Instrum. Methods Phys. Res.* **222**, 121–127.
Ice, G. E. & Sparks, C. J. (1994). *J. Opt. Soc. Am. A*, **11**, 1265–1271.
International Tables for Crystallography (2002). Volume A, edited by T. Hahn, pp. 696–698. Dordrecht: Kluwer.
Koshelev, I., Huang, R., Graber, T., Meron, M., Muir, L., Lavender, W., Battaile, K., Mulichak, A. M. & Keefe, L. J. (2007). *AIP Conf. Proc.* **879**, 840–843.
Kushnir, V., Quintana, J. & Georgopoulus, P. (1993). *Nucl. Instrum. Methods Phys. Res. A*, **328**, 588–591.
Lang, J. C., Srajer, G., Wang, J. & Lee, P. L. (1999). *Rev. Sci. Instrum.* **70**, 4457–4461.
Maj, J., Waldschmidt, G., Macrander, A., Koshelev, I., Huang, R., Maj, L. & Maj, A. (2006). *Adv. X-ray Anal.* **48**, 176–182.
Margaritondo, G. (1988). *Introduction to Synchrotron Radiation*, pp. 34–37. Oxford University Press.
Padmore, H., Howells, M. R. & Iric, S. (1996). *Proc. SPIE*, **2856**, 145–156.
Pohl, E., González, A., Hermes, C. & van Silfhout, R. G. (2001). *J. Synchrotron Rad.* **8**, 1113–1120.
Rosenbaum, G. *et al.* (2006). *J. Synchrotron Rad.* **13**, 30–45.
Rosenbaum, G., Sullivan, M., Fischetti, R. & Rock, L. (1992). *Rev. Sci. Instrum.* **63**, 931.
Roth, M., Carpentier, P., Kaïkati, O., Joly, J., Charrault, P., Pirocchi, M., Kahn, R., Fanchon, E., Jacquamet, L., Borel, F., Bertoni, A., Israel-Gouy, P. & Ferrer, J.-L. (2002). *Acta Cryst.* D**58**, 805–814.
Schwinger, J. (1949). *Phys. Rev.* **75**, 1912–1925.
Sparks, C. J., Borie, B. S. & Hastings, J. B. (1980). *Nucl. Instrum. Methods*, **172**, 237–242.
Sparks, C. J., Ice, G. E., Wong, J. & Batterman, B. (1981). *Nucl. Instrum. Methods Phys. Res.* **195**, 73–78.
Timoshenko, S. & Woinowsky-Krieger, S. (1959). *Theory of Plates and Shells*, pp. 1–6, 33–47. York: The Maple Press Company.
Underwood, J. H. (1977). *Space Sci. Instrum.* **3**, 259–270.
Wang, J., Toby, B., Lee, P., Ribaud, L., Antao, S., Kurtz, C., Ramanathan, M., Von Dreele, R. & Beno, M. (2008). *Rev. Sci. Instrum.* **79**, 085105.